

Continuous gravitational waves from thermal mountains on accreting neutron stars: effect of the nuclear pasta phase

HONG-BO LI,¹ LIJING SHAO,^{1,2} CHENG-JUN XIA,³ AND REN-XIN XU^{4,1}

¹*Kavli Institute for Astronomy and Astrophysics, Peking University, Beijing 100871, China*

²*National Astronomical Observatories, Chinese Academy of Sciences, Beijing 100012, China*

³*Center for Gravitation and Cosmology, College of Physical Science and Technology, Yangzhou University, Yangzhou 225009, China*

⁴*Department of Astronomy, School of Physics, Peking University, Beijing 100871, China*

ABSTRACT

As density increases, the shape of nuclei transitions to non-spherical “nuclear pasta” structures. The physical properties of the nuclear pasta, such as thermal conductivity and elasticity, have implications for detecting continuous gravitational waves from a rapidly rotating neutron star. In this work, we investigate the effect of the nuclear pasta on the quadruple moment, and find out that, compared with previous work, the quadrupole moment contributing to continuous gravitational-wave radiation can be up to two orders of magnitude larger. We also discuss the relationship between the quadrupole moment and the maximum shear strain. Considering the properties of nuclear pasta, we study the detectability of known accreting neutron stars and compare predicted results to the detectable amplitude limits. These sources are well above the sensitivity curves for Cosmic Explorer and Einstein Telescope detectors. Our work advances the understanding of the properties of nuclear pasta and a possible mechanism for continuous gravitational waves.

Keywords: Neutron stars (1108); Low-mass x-ray binary stars (939); Gravitational waves (678)

1. INTRODUCTION

Spinning non-axisymmetric neutron stars (NSs) are promising sources of continuous gravitational waves (CGWs) via quadrupole radiation (see Riles 2023; Wette 2023; Jones & Riles 2024, for a detailed review). The characteristic amplitude of CGW signal scales with the square of the rotation frequency, combined with the noise curve of ground-based detectors, making the more rapidly rotating NSs ideal candidates for detection. The detection strategies for CGWs from rapidly rotating NSs mainly fall into two categories: targeted observation of accreting millisecond X-ray pulsars (AMXPs; Abbott et al. 2005, 2007a; Abadie et al. 2011; Abbott et al. 2022a); all-sky searches for CGWs from unobserved sources (Abbott et al. 2007a, 2017a, 2019, 2021, 2022b; Steltner et al. 2023; Tripathy & Riles 2024). Although CGWs from NSs have yet to be detected, the upper limit of the amplitude and ellipticity are becoming more strictly limited.

Low-mass X-ray binaries (LMXBs) were originally invoked as a strong source of CGWs to explain an observational puzzle. Observation of NSs in LMXBs has shown that spins are far below the predicted breakup limit of 1000 Hz (Cook et al. 1994; Lattimer & Prakash 2007).

For instance, the fastest-spinning accreting pulsar observed to date is IGR J00291+5934 that spins at 599 Hz (Galloway et al. 2005). The statistical evidence about the spin distributions has been discussed by Patruno et al. (2017). They found the distribution to comprise two sub-populations: one at relatively low spin frequencies with an average of ≈ 300 Hz and the other at higher frequencies with an average of ≈ 575 Hz. In particular, the spin frequency has a statistical cut-off approaching to 730 Hz (Chakrabarty et al. 2003; Patruno 2010). The candidate mechanisms are divided into two camps. The first is the interaction between the accretion disc and the magnetosphere of NS (Ghosh & Lamb 1978; White & Zhang 1997; Andersson et al. 2005). The second possible scenario is that CGW may provide the torque needed to balance the accretion torque (Papaloizou & Pringle 1978; Wagoner 1984; Bildsten 1998). The latter scenario is our main focus in the present work.

Many possible mechanisms may lead to CGW emission. These include: (i) the r -mode instability (Andersson et al. 1999; Levin 1999; Heyl 2002; Mahmoodifar & Strohmayer 2013; Pi et al. 2015); (ii) free precession (Jones & Andersson 2002; Van Den Broeck 2005; Gao et al. 2020, 2023); (iii) non-axisymmetric deforma-

tions of the NS crust, including magnetic deformation (Melatos & Payne 2005; Haskell et al. 2008; Fujisawa et al. 2022), elastic deformations in the crust (Bildsten 1998; Ushomirsky et al. 2000; Haskell et al. 2006; Gittins et al. 2020), and other forms (Yim et al. 2023, 2024). The associated non-axisymmetric deformations of NSs are commonly referred to as “magnetic mountains” or “thermal mountains”.

It is considered that the NS crust exists from the bottom of the ocean layer with a density in the range of 10^6 – 10^9 g cm^{-3} inwards to the boundary with a fluid core at a density of the order of the saturation density of nuclear matter, $\rho_s \approx 2.6 \times 10^{14}$ g cm^{-3} . As density increases, the shape of the nuclear matter region changes from sphere to non-spherical, which is known as “pasta structure” (see Caplan & Horowitz 2017; Lopez et al. 2021, for a detailed review). The physical properties of the nuclear pasta, such as thermal conductivity and elasticity, have implications for the explanation of cooling curves for MXB 1659–29 (Horowitz et al. 2015) and of the maximum value for a spin period of isolated X-ray pulsars (Pons et al. 2013). Considering the effect of nuclear pasta, Sotani (2011) calculated the torsional shear mode, which is dependent on the shear modulus, and explained the quasi-periodic oscillations in SGR 1806–20.

For the scenario of the elastic mountains, previous works have ignored the physical properties of the nuclear pasta and also have not discussed the effect of the nuclear pasta on the quadrupole moment (Bildsten 1998; Ushomirsky et al. 2000; Haskell et al. 2006; Gittins et al. 2020). Hence, in this paper, we investigate the physical properties mentioned above, including thermal conductivity and elasticity. Considering the effect of the thermal conductivity for a nuclear pasta, we calculate the temperature asymmetry in the accreted crust. Next, we calculate the quadrupole moment, Q_{22} , using the crust perturbation equations and compare our predicted results to the detectable amplitude limits. Finally, we discuss the relationship between Q_{22} and the maximum shear strain.

The paper is organized as follows. In Sec. 2, we compute the hydrostatic structure of an accreting NS for accreted crustal EOS (as described by Haensel & Zdunik 1990a,b). The thermal structure of a spherically symmetric NS is presented in Sec. 3. Based on the background solutions, in Sec. 4, we integrate the thermal perturbation equations to determine the magnitude of the temperature variations. In Sec. 5, we calculate the elastic deformation of the accreted crust and compare predicted results to the detectable amplitudes. In Sec. 6, we calculate the maximum values for shear strain and discuss the relationship between the quadrupole moment

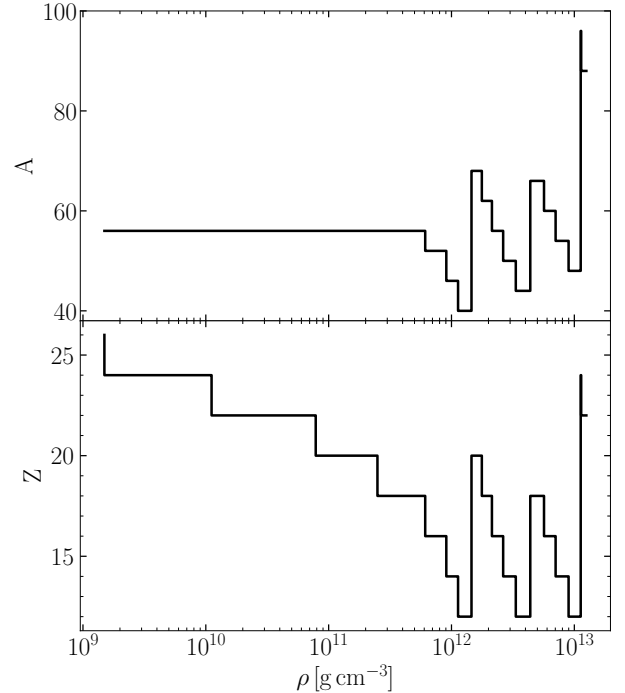


Figure 1. Mass number A (top) and nuclear charge Z (bottom) with increasing density. The data are taken from Table 2 of Haensel & Zdunik (1990a).

and maximum shear strain. Finally, we summarize and discuss our results in Sec. 7.

2. STRUCTURE OF AN ACCRETING NEUTRON STAR

To construct the hydrostatic structure of an accreting NS, we choose the EOS DH (Douchin & Haensel 2001), which describes the core, and use the model of EOS HZ (Haensel & Zdunik 1990a,b) in the accreted crust. We calculate the structure of the crust by employing Newtonian gravity. Haensel & Zdunik (1990a) have studied the evolution of composition in the accreted crust and provided tabulated EOS data in detail. For illustration, we plot the mass number A and nuclear charge Z as a function of the density in Fig. 1.

Strictly speaking, the capture layers have a finite thickness. The thickness of the capture layers was calculated by Ushomirsky et al. (2000). However, we follow the approach of Osborne & Jones (2020) and Hutchins & Jones (2023), who assume that the transitions between capture layers are infinitely sharp and smear the heat released at each transition over shells of constant (A, Z) . This approximation was used to model crustal heating of an accreting NS (Brown 2000; Brown & Cumming 2009).

Following Osborne & Jones (2020), we calculate the mass and radius of the core using the TOV equations

and obtain the mass and thickness of the accreted crust employing Newtonian theory. The transition density of the interface between the core and crust is $\rho = 1.25 \times 10^{13} \text{ erg cm}^{-3}$, and the transition density of the interface between the crust and ocean is $\rho = 1.49 \times 10^9 \text{ erg cm}^{-3}$.

In the present work, we mainly consider the physical properties of the nuclear pasta so that the transition density of the interface between the core and nuclear pasta is $\rho = 1.28 \times 10^{14} \text{ erg cm}^{-3}$. The normal crust density ranges from $1.25 \times 10^{13} \text{ erg cm}^{-3}$ to $1.49 \times 10^9 \text{ erg cm}^{-3}$. In the following thermal calculations, we will restrict our computational domain to a range of densities (Haensel & Zdunik 1990a), appending the density ranges of the nuclear pasta. Similarly, we calculate the mass and radius of the nuclear pasta and accreted crust using Newtonian theory. Hence, the density and radius at the bottom of the nuclear pasta are

$$\rho_{\text{I}} = 1.28 \times 10^{14} \text{ erg cm}^{-3}, \quad (1)$$

$$R_{\text{I}} = 10.69 \text{ km}, \quad (2)$$

and at the interface between the nuclear pasta and normal crust are

$$\rho_{\text{II}} = 1.25 \times 10^{13} \text{ erg cm}^{-3}, \quad (3)$$

$$R_{\text{II}} = 11.12 \text{ km}, \quad (4)$$

and at the interface between the crust and the ocean are

$$\rho_{\text{III}} = 1.49 \times 10^9 \text{ erg cm}^{-3}, \quad (5)$$

$$R_{\text{III}} = 11.89 \text{ km}. \quad (6)$$

The density profile with central density $\rho_c = 1.496 \times 10^{15} \text{ g cm}^{-3}$ for our model is shown in Fig. 2. This model has a mass of $1.84 M_{\odot}$ and a nuclear pasta thickness of 0.43 km and a crust thickness of 0.77 km.

Because the EOS of NS is usually weakly dependent on temperature, the calculation of the thermal structure is decoupled from the hydrostatic calculation. The crust temperature is proportional to the accretion rates. For a higher accretion rate, the thermal energy is larger than the Coulomb energy and leads to the melting of the accreted crust (Brown 2000; Ushomirsky et al. 2000). The ratio of Coulomb energy to thermal energy is defined by

$$\Gamma \equiv \frac{(Ze)^2}{k_{\text{B}}T} \left(\frac{4\pi n_{\text{ion}}}{3} \right)^{1/3}, \quad (7)$$

where n_{ion} is the ion number density, and k_{B} is the Boltzmann's constant. The crystallization point occurs at $\Gamma = 175$ (Haensel et al. 2007). We assume that the ratio value exceeds 175, that is, the crust and pasta phase are solid in our model.

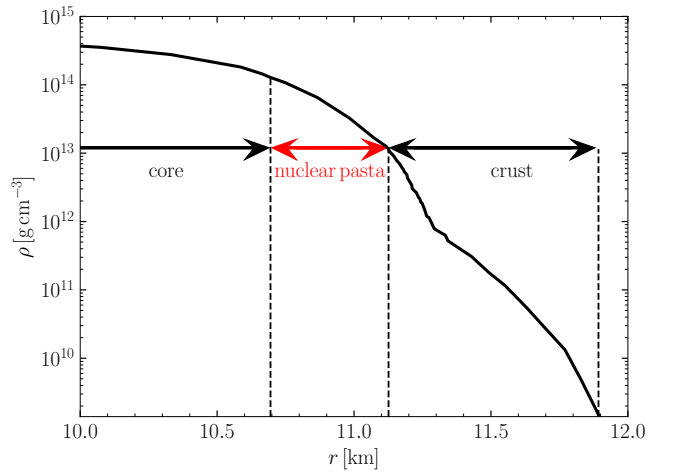


Figure 2. Density as a function of radius, with a central density of $\rho_c = 1.496 \times 10^{15} \text{ g cm}^{-3}$. This model represents a NS with mass of $1.84 M_{\odot}$ and includes a nuclear pasta thickness of 0.43 km and a crust thickness of 0.77 km.

3. THERMAL STRUCTURE OF AN ACCRETING NEUTRON STAR

In this section, we calculate a steady-state thermal structure based on the Newtonian formulation (Ushomirsky et al. 2000; Osborne & Jones 2020; Hutchins & Jones 2023). The temperature profile is spherically symmetric and independent of the time. From energy conservation, the heat flux \mathbf{F} is related to the net rate of heat energy generation per unit volume Q via

$$\nabla \cdot \mathbf{F} = Q = Q_{\text{nuc}} - Q_{\text{neu}}, \quad (8)$$

where Q_{nuc} is the local energy deposited via nuclear reactions, and Q_{neu} is the local energy loss due to neutrino emission. The heat flux is related to the temperature T by the Fourier's law,

$$\mathbf{F} = -\kappa \nabla T, \quad (9)$$

where κ is the thermal conductivity. Assuming the background structure is spherically symmetric, the heat flux only depends on the radial coordinate r . We can obtain the following system of equations for the heat flux F and temperature T ,

$$\frac{dF}{dr} = Q - \frac{2}{r}F, \quad (10)$$

$$\frac{dT}{dr} = -\frac{1}{\kappa}F. \quad (11)$$

To solve the above equations, we will consider the description of the heating term Q_{nuc} , neutrino cooling Q_{neu} , thermal conductivity, and the boundary conditions at each end of the integration. These aspects will be discussed in detail in the following subsections.

3.1. Accretion heating

In the regions of the crust, we use the EOS HZ model to describe an accreted crust. The values of mass number A , nuclear charge Z , electron chemical potential μ_e , and the mass fraction of free neutrons X_n are listed in Table 2 of [Haensel & Zdunik \(1990a\)](#). This is important as the nuclear composition changes in discrete steps with increasing density, corresponding to different electron capture layers.

As the material moves deeper into the crust, electron capture reactions begin to occur at a constant pressure, depositing heat into the crust ([Haensel & Zdunik 1990b](#)). The heat deposited in each electron capture layer per unit volume per unit time depends on the accretion rate \dot{M} . The heat released in each capture layer is by smearing the heat deposited over whole shells as ([Hutchins & Jones 2023](#)),

$$Q_{\text{nuc}}^{\text{crust}} = \frac{\dot{M}\epsilon_{\text{nuc}}}{\frac{4}{3}\pi(r_i^3 - r_{i+1}^3)}, \quad (12)$$

where ϵ_{nuc} is the heat deposited per nucleon by the relevant nuclear reaction, and r_i is the radii at the i^{th} capture layer.

In the regions of nuclear pasta, we adopt the model of EOS DH, which describes a non-accreted NS. The heat deposited per nucleon is $\epsilon_{\text{nuc}} = 0$, meaning $Q_{\text{nuc}}^{\text{pasta}} = 0$. In our calculation, we only use the value of pressure P and density ρ to obtain the thickness of the nuclear pasta.

3.2. Neutrino cooling

In the regions of the crust, the neutrino luminosity is dominated by the electron-ion bremsstrahlung ([Brown 2000](#)). The local energy loss due to neutrino emission $Q_{\text{neu}}^{\text{crust}}$ is given by ([Haensel et al. 1996](#))

$$Q_{\text{neu}}^{\text{crust}} = 3.229 \times 10^{17} \rho_{12} T_9^6 \frac{Z^2}{A} (1 - X_n) \text{ erg s}^{-1} \text{ cm}^{-3}, \quad (13)$$

where $\rho_{12} = \rho/10^{12} \text{ g cm}^{-3}$ and $T_9 = T/10^9 \text{ K}$.

[Lin et al. \(2020\)](#) have discussed the fast neutrino cooling of nuclear pasta, using the molecular dynamic simulations. The value of the neutrino luminosity is $Q_{\text{neu}}^{\text{pasta}} \approx 8 \times 10^{21} T_9^8 \text{ erg s}^{-1} \text{ cm}^{-3}$. However, in the present work, we assume that the electron-ion bremsstrahlung is still dominant but independent on A , Z , and X_n . The local energy loss due to neutrino emission, $Q_{\text{neu}}^{\text{pasta}}$, can be approximated by

$$Q_{\text{neu}}^{\text{pasta}} \approx 3 \times 10^{17} \rho_{12} T_9^6 \text{ erg s}^{-1} \text{ cm}^{-3}. \quad (14)$$

3.3. Thermal conductivity

The thermal conductivity in the crust helps determine the temperature profile and heat flux, which is very important for the cooling and transport properties of the NS ([Potekhin et al. 2015](#)). Using the results of [Yakovlev et al. \(2001\)](#), the conductivity can be written as

$$\kappa^{\text{crust}} = \frac{\pi^2 k_B^2 T n_e}{3 m_e^*} \tau. \quad (15)$$

Here n_e is the electron number density, m_e^* is the effective electron mass, and $\tau = 1/\nu$ is the relaxation time with ν the scattering frequency of the different mechanisms. In the regions of the crust, the scattering frequency ν is determined as

$$\nu = \nu_{\text{ep}} + \nu_{\text{eQ}}, \quad (16)$$

where ν_{ep} and ν_{eQ} are the scattering frequencies for the electron-phonon and electron-impurity, respectively. We neglect the term of the electron-electron scattering frequency because the strong degeneracy of the electrons restricts the available phase space ([Brown 2000](#)).

We follow the formalism of [Yakovlev & Urpin \(1980\)](#), and the electron-phonon scattering is temperature dependent as

$$\nu_{\text{ep}} = \frac{12e^2 k_B T}{\hbar^2 c}. \quad (17)$$

As the density increases, electron-impurity scattering becomes more important, and the scattering frequency is written as

$$\nu_{\text{eQ}} = \frac{4\pi Q_{\text{imp}} e^4 n_{\text{ion}}}{p_F^2 v_F} \Lambda_{\text{imp}}, \quad (18)$$

where p_F and v_F are the momentum and velocity of electrons at the Fermi surface and $\Lambda_{\text{imp}} = 1$ is the logarithmic Coulomb factor, and the impurity parameter is defined by

$$Q_{\text{imp}} \equiv n_{\text{ion}}^{-1} \sum_i n_i (Z_i - \langle Z \rangle)^2. \quad (19)$$

Here, the sum i is over all the different species of ions, with atomic number Z_i and mean atomic number $\langle Z \rangle$. The impurity parameter in the accreted crust remains highly uncertain. Observational results of the cooling NS transient MXB 1659–29 indicate that the impurity parameter was constrained to $Q_{\text{imp}} < 10$ ([Brown & Cumming 2009](#)). However, [Ootes et al. \(2019\)](#) investigated the long-term temperature evolution of a transiently accreting NS and suggested that the impurity parameter can range from 30 to 100.

We next briefly review the thermal conductivity of nuclear pasta. [Horowitz & Berry \(2008\)](#) investigated the thermal conductivity of nuclear pasta using

molecular dynamics simulations, and they found that the thermal conductivity lies in the range of $10^{20} \sim 10^{21} \text{ erg K}^{-1} \text{ cm}^{-1} \text{ s}^{-1}$. Note that this value is from electrons. Topological defects in nuclear pasta can reduce the thermal conductivity by up to an order of magnitude (Schneider et al. 2016). Deibel et al. (2017) studied the observed late-time cooling of MXB 1659–29 and pointed out that it is consistent with low thermal conductivity for nuclear pasta, with a value of $10^{17} \text{ erg K}^{-1} \text{ cm}^{-1} \text{ s}^{-1}$. The thermal conductivity of nuclear pasta is expected to be sensitive to the temperature and fraction of species (see Nandi & Schramm 2018; Dorso et al. 2020; Caplan et al. 2021, and references therein). In this work, we adopt the following formalism of the thermal conductivity for nuclear pasta,

$$\kappa^{\text{pasta}} \approx 3 \times 10^{19} \left(\frac{T}{T_8} \right) \text{ erg K}^{-1} \text{ cm}^{-1} \text{ s}^{-1}. \quad (20)$$

The effect of the thermal conductivity of nuclear pasta on the temperature profiles and heat flux is discussed in Sec. 3.5.

3.4. Boundary conditions

In this subsection, we describe the boundary conditions to solve Eqs. (10) and (11). The bottom boundary is the interface between core and crust or nuclear pasta. We assume that the core is isothermal, maintaining the same temperature as the bottom boundary. The bottom boundary can be written as

$$F_{\text{bottom}} = -\frac{L_{\text{core}}}{4\pi R_{\text{bottom}}}, \quad (21)$$

where R_{bottom} is the radius of NS core. The neutrino luminosity of the core due to the modified Urca formula is (Shapiro & Teukolsky 1983)

$$L_{\text{core}} = 5.93 \times 10^{39} \text{ erg s}^{-1} \left(\frac{M}{M_{\odot}} \right) \left(\frac{\rho_{\text{nuc}}}{\rho} \right)^{1/3} T_8^8 \exp\left(-\frac{\Delta}{k_B T_{\text{bottom}}}\right), \quad (22)$$

where ρ_{nuc} is nuclear density. In this work, we only consider the normal core, for which $\Delta = 0$. The case of the superfluid core will be addressed in future calculations.

The top boundary is set to the steady burning temperature of the hydrogen/helium burning layer and the accretion as

$$T_{\text{top}} \approx 5.3 \times 10^8 \text{ K} \left(\frac{\dot{m}}{\dot{m}_{\text{Edd}}} \right)^{2/7}, \quad (23)$$

where \dot{m} is the local accretion rate (Schatz et al. 1999) and \dot{m}_{Edd} is the local Eddington limit. In the following calculations, we assume the uniform accretion over the surface of NS and parameterize our results in terms of the global accretion rate, \dot{M} .

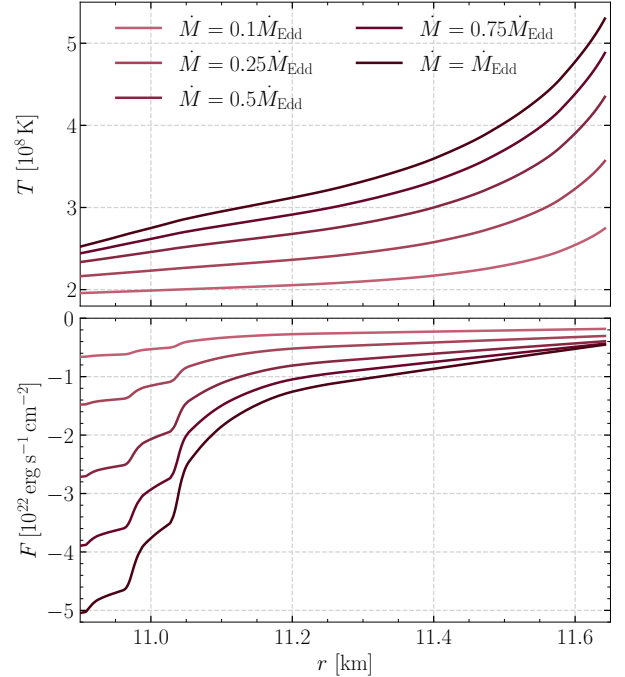


Figure 3. The upper panel shows the temperature profiles against the radius without the pasta phase. Different accretion rates are chosen. The lower panel shows the heat flux versus the radius. We set the impurity parameter $Q_{\text{imp}} = 1$.

3.5. Results: Background thermal structure

In the upper panel of Fig. 3, we show the temperature distributions without nuclear pasta. As the accretion rate increases, the temperature variation becomes more significant. The temperature gradient is positive, indicating an inwards flow of heat throughout the entire crust. In the lower panel of Fig. 3, we show the heat flux against the radius. One notices that the heat flux is negative, which means that heat is flowing toward the core.

Based on the observational constraints, we set the value of the impurity parameter $Q_{\text{imp}} = 1$ to calculate the temperature profiles and heat flux. However, as mentioned above, the impurity parameter is highly uncertain. For example, $Q_{\text{imp}} \sim 100$ is typical of the mixture from the ashes of steady state burning (Schatz et al. 1999).

In Fig. 4, we show the temperature profiles and heat flux for different values of Q_{imp} . When $Q_{\text{imp}} \lesssim 10$, these results are insensitive to the impurity parameter, when $Q_{\text{imp}} \sim 100$, large differences appear in the profiles of the temperature and heat flux, because Q_{imp} quantifies the thermal conductivity of the crust, which is dominated by electron-impurity scattering. The thermal conductivity in the crust decreases with increasing impurity parameters. This reduces heat conduction from the

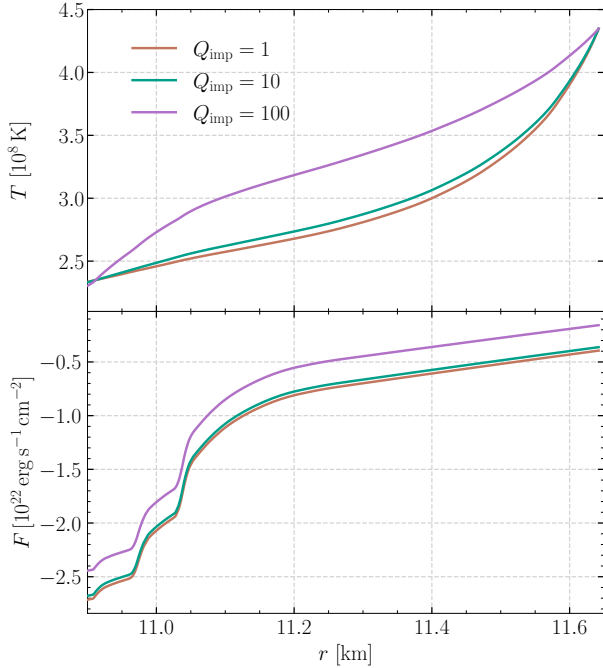


Figure 4. Temperature profiles (*upper*) and heat flux (*lower*) for different impurity parameters without nuclear pasta. The accretion rate $\dot{M} = 0.5\dot{M}_{\text{Edd}}$.

crust to the core, resulting in a higher crust temperature and increasing cooling through crustal neutrino emission.

Considering various accretion rates and impurity parameters, we plot the temperature profiles with nuclear pasta against the radius in Figs. 5 and 6. We find that the temperature decreases with depth in the crust, extending the region of the nuclear pasta. The temperature profile is insensitive to the impurity parameter in the region of the nuclear pasta.

4. TEMPERATURE PERTURBATION DUE TO PHYSICAL ASYMMETRIES

To calculate lateral temperature variation, δT , we consider the following two possible causes. First, the heat deposited, ϵ_{nuc} , has lateral variation owing to the nuclear transmutation of different elements depositing different amounts of energy. The lateral variations of this type are represented by $f_{\text{nuc}} = \delta\epsilon_{\text{nuc}}/\epsilon_{\text{nuc}}$. Second, the charge-to-mass ratio, Z^2/A , may differ if the process of nuclear burning is different on different sides of the star. The crust conductivity scales as $\kappa^{\text{crust}} \propto (Z^2/A)^{-1}\rho T^{n_k}$, where $n_k = 1$ (Schatz et al. 1999; Ushomirsky et al. 2000), and neutrino emission scales as $Q_{\text{neu}}^{\text{crust}} \propto (Z^2/A)\rho T^{n_e}$, where $n_e = 6$ (see Eq. 13 in this paper). Using the results of Ushomirsky et al. (2000), we define the perturbation of charge to mass ratio as $f_{\text{comp}} = \delta(Z^2/A)/(Z^2/A)$. The calculation of δT de-

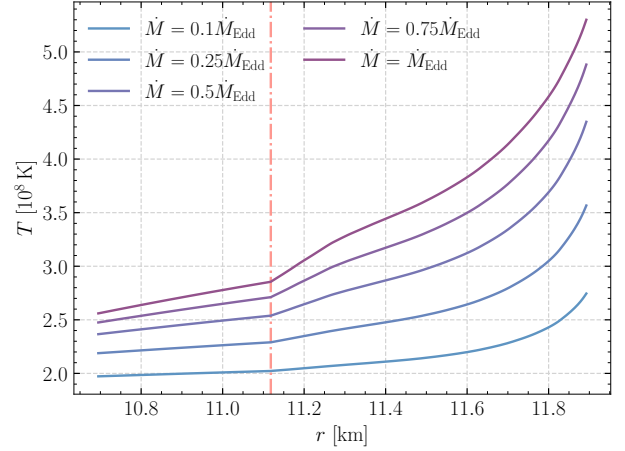


Figure 5. Temperature profiles versus the radius with pasta phase for different accretion rates. The impurity parameter is $Q_{\text{imp}} = 1$. The vertical dash-dotted line is the nuclear pasta-crust interface.

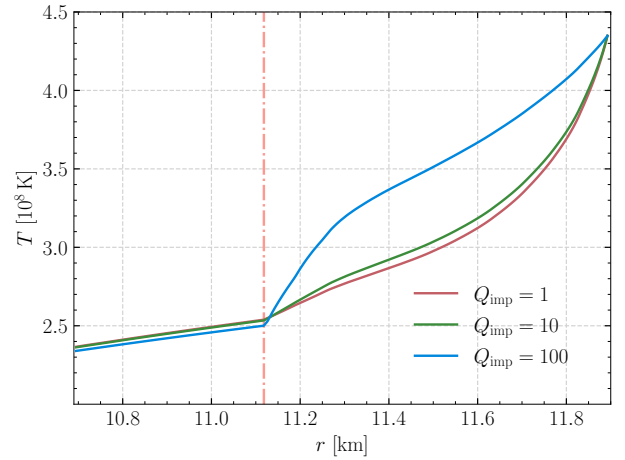


Figure 6. Temperature profiles for different impurity parameters with nuclear pasta. The accretion rate is $\dot{M} = 0.5\dot{M}_{\text{Edd}}$. The vertical dash-dotted line has the same meaning as in Fig. 5.

pends on f_{nuc} and f_{comp} in the accreted crust. In the nuclear pasta regions, $f_{\text{nuc}} = f_{\text{comp}} = 0$, but the neutrino emission energy $Q_{\text{neu}}^{\text{pasta}}$ and thermal conductivity κ^{pasta} can affect the lateral temperature variation δT . Detailed results are shown in Sec. 4.2.

4.1. The thermal perturbation equations

We assume that the angular dependence is given by the spherical harmonic function $Y_{\ell m}$. The temperature perturbative variable can be written as $\delta T(r, \theta, \phi) = \delta T(r)Y_{\ell m}$. We can obtain the following radial perturbation equation (see Ushomirsky et al. 2000, for a detailed

variational derivation),

$$\begin{aligned} & \frac{1}{r^2} \frac{d}{dr} \left(r^2 \kappa \frac{d\delta T}{dr} \right) - n_k \frac{F}{\kappa T} \kappa \frac{d\delta T}{dr} - \ell(\ell+1) \frac{\kappa \delta T}{r^2} \\ & - \left\{ n_k \frac{F^2}{\kappa T} + \rho \left[n_k (Q_{\text{nuc}} - Q_{\text{neu}}) + n_e Q_{\text{neu}} \right] \right\} \frac{\delta T}{T} \\ & = \rho \left\{ f_{\text{comp}} (2Q_{\text{neu}} - Q_{\text{nuc}}) - f_{\text{nuc}} Q_{\text{nuc}} \right\}. \end{aligned} \quad (24)$$

For the case without nuclear pasta, we use the same boundary conditions as in Ushomirsky et al. (2000). The temperature perturbation vanishes at the top and the bottom of the crust. For the case of nuclear pasta, the temperature perturbation $\delta T = 0$ extends to the bottom of the nuclear pasta.

An important issue to clarify is the role of the core. The thermal conductivity of the core is higher than that of the crust of the NS (Baiko et al. 2001), and the temperature perturbation in the core is significantly smaller than in the crust and pasta phase. Therefore, we can approximate the core as perfectly conducting and isothermal.

4.2. Results: perturbed thermal structure

In the left panel of Fig 7, we plot the temperature perturbations as a function of the radius for different accretion rates. The results from the lateral variations of nuclear heating, with $f_{\text{nuc}} = 0.1$ and $f_{\text{comp}} = 0$, indicate that the conductivity and neutrino emission are unperturbed. We have set $Q_{\text{imp}} = 1$ and $\ell = 2$. The typical values of $\delta T/T$ are a few times 1% in the crust. In the right panel of Fig. 7, we show the temperature perturbations versus the radius for different impurity parameters. As the impurity parameter increases, the temperature perturbations become larger.

To better understand the effect of nuclear pasta, we give our results in Fig. 8. The size of the temperature perturbations increases with higher accretion rates \dot{M} and impurity parameters Q_{imp} . The maximal values of $\delta T/T$ increase by a factor of two.

5. THE ELASTIC DEFORMATION OF THE CRUST

When a star deforms from a perfect sphericity, it develops multipole moments. These are defined as

$$Q_{\ell m} \equiv \int_0^R \delta \rho_{\ell m}(r) r^{\ell+2} dr, \quad (25)$$

where (ℓ, m) denotes the harmonic mode of the density perturbation $\delta \rho_{\ell m}(r)$, and R is the stellar radius. The quadrupole moment with $(\ell, m) = (2, 2)$ contributes to the CGW signal. Bildsten (1998) pointed out that the spin-up torque from accretions is balanced by the emission of quadrupolar gravitational radiation. Under the

condition for torque balance, the CGWs amplitude can be written as (Ushomirsky et al. 2000)

$$h_0 = \frac{32\pi}{5} \left(\frac{\pi}{3} \right)^{1/2} \frac{G}{c^4} \frac{Q_{22} f_{\text{GW}}^2}{d}, \quad (26)$$

where G and c are the speed of light and the gravitational constant, respectively, d is the distance of the source, and the gravitational wave (GW) frequency is $f_{\text{GW}}^2 = 2\nu$ for a NS rotating with spin frequency ν (Abbott et al. 2019; Reed et al. 2021).

5.1. The crustal perturbation equations

Following Ushomirsky et al. (2000), the perturbed Euler equation for NSs with an elastic crust in the Cowling approximation is written as

$$0 = -\nabla_i \delta P - \delta \rho \nabla_i \Phi + \nabla^j t_{ij}, \quad (27)$$

where Φ is the gravitational potential, and the shear-stress tensor t_{ij} describes elastic forces as a first-order perturbation. In our calculation, the shear-stress tensor t_{ij} can be written as

$$t_{ij} = \mu \left(\nabla_i \xi_j + \nabla_j \xi_i - \frac{2}{3} g_{ij} \nabla_k \xi^k \right), \quad (28)$$

where g_{ij} is the flat three-metric, and the shear modulus μ in the crust is,

$$\mu^{\text{crust}} = 0.1194 \frac{n_{\text{ion}} (Ze)^2}{a}, \quad (29)$$

where $a = [3/(4\pi n_{\text{ion}})]^{1/3}$ is the average ion spacing. In particular, for the elastic properties of the nuclear pasta that was described by Caplan et al. (2018), Pethick et al. (2020), and Xia et al. (2023), the shear modulus could be $\mu^{\text{pasta}} \approx 10^{30} \text{ erg cm}^{-3}$.

Employing tensor spherical harmonics leads to a convenient decomposition of the shear-stress tensor (Ushomirsky et al. 2000; Haskell et al. 2006),

$$\begin{aligned} t_{ij} = & t_{rr} Y_{\ell m} (\nabla_i r \nabla_j r - \frac{1}{2} e_{ij}) + t_{r\perp}(r) f_{ij} \\ & + t_{\Lambda}(r) (\Lambda_{ij} + \frac{1}{2} Y_{\ell m} e_{ij}), \end{aligned} \quad (30)$$

where t_{rr} , $t_{r\perp}$, and t_{Λ} are functions of radial coordinate r , $\beta = \sqrt{\ell(\ell+1)}$ (Ushomirsky et al. 2000; Haskell et al. 2006),

$$e_{ij} = g_{ij} - \nabla_i r \nabla_j r, \quad (31)$$

$$f_{ij} = \frac{r}{\beta} (\nabla_i r \nabla_j Y_{\ell m} + \nabla_j r \nabla_i Y_{\ell m}), \quad (32)$$

$$\Lambda_{ij} = \left(\frac{r}{\beta} \right)^2 \nabla_i \nabla_j Y_{\ell m} + \frac{1}{\beta} f_{ij}. \quad (33)$$

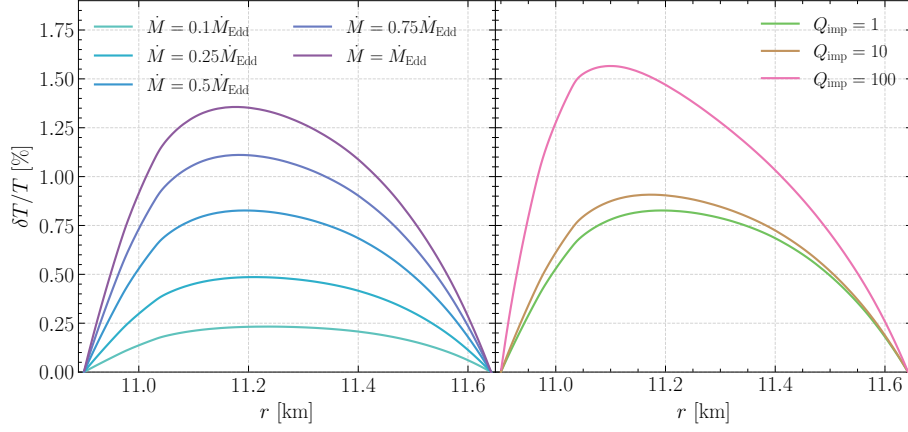


Figure 7. Temperature perturbations in the crust for different accretion rates with a fixed impurity parameter $Q_{\text{imp}} = 1$ (left) and for impurity parameter with a fixed accretion rate $\dot{M} = 0.5\dot{M}_{\text{Edd}}$ (right). Both panels have $f_{\text{nuc}} = 0.1$, $f_{\text{comp}} = 0$, and $\ell = 2$.

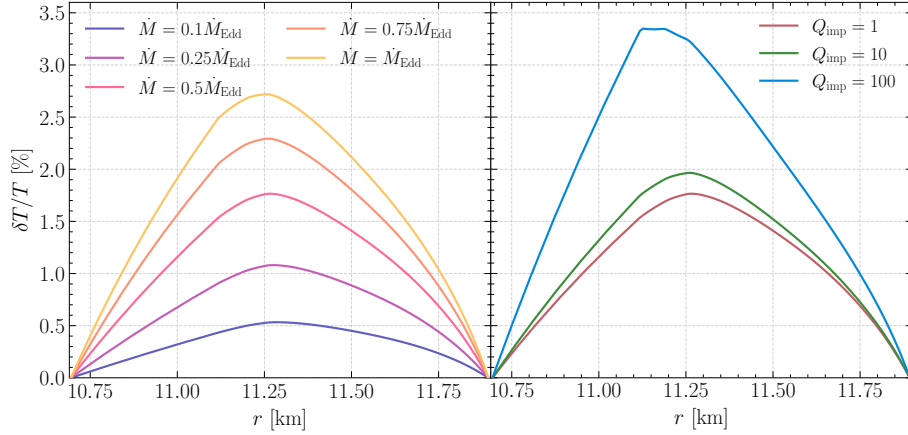


Figure 8. Same as Fig. 7, but for the effect of nuclear pasta.

The displacement vector ξ^i is associated with polar perturbations, and it is given by,

$$\xi^i = \xi_r(r) \nabla^i r Y_{\ell m} + \frac{r}{\beta} \xi_{\perp}(r) \nabla^i Y_{\ell m}, \quad (34)$$

where $\xi_r(r)$ and $\xi_{\perp}(r)$ are the radial and tangential components of the displacement, respectively. Again, the perturbed continuity equation is determined as

$$\delta\rho = -\rho \frac{\partial \xi_r}{\partial r} - \left(\frac{2\rho}{r} + \frac{\partial \rho}{\partial r} \right) \xi_r + \beta \rho \frac{\xi_{\perp}}{r}. \quad (35)$$

Using four new variables (Ushomirsky et al. 2000)

$$z_1 = \frac{\xi_r}{r}, \quad (36)$$

$$z_2 = \frac{t_{rr}}{P} - z_1 \frac{d \ln P}{d \ln r}, \quad (37)$$

$$z_3 = \frac{\xi_{\perp}(r)}{\beta r}, \quad (38)$$

$$z_4 = \frac{t_{r\perp}}{\beta P}, \quad (39)$$

we obtain the following set of coupled ordinary differential equations (ODEs) (Ushomirsky et al. 2000),

$$\begin{aligned} \frac{dz_1}{d \ln r} = & - \left(1 + 2 \frac{\alpha_2}{\alpha_3} - \frac{\alpha_4}{\alpha_3} \right) z_1 + \frac{1}{\alpha_3} z_2 \\ & + \ell(\ell+1) \frac{\alpha_2}{\alpha_3} z_3 + \frac{1}{\alpha_3} \Delta S, \end{aligned} \quad (40)$$

$$\begin{aligned} \frac{dz_2}{d \ln r} = & \left(UV - 4V + 12\Gamma \frac{\alpha_1}{\alpha_3} - 4 \frac{\alpha_1 \alpha_4}{\alpha_3} \right) z_1 \\ & + \left(V - 4 \frac{\alpha_1}{\alpha_3} \right) z_2 + \ell(\ell+1) \left(V - 6\Gamma \frac{\alpha_1}{\alpha_3} \right) z_3 \\ & + \ell(\ell+1) z_4 - 4 \frac{\alpha_1}{\alpha_3} \Delta S, \end{aligned} \quad (41)$$

$$\frac{dz_3}{d \ln r} = -z_1 + \frac{1}{\alpha_1} z_4, \quad (42)$$

$$\begin{aligned} \frac{dz_4}{d \ln r} = & \left(V - 6\Gamma \frac{\alpha_1}{\alpha_3} + 2 \frac{\alpha_1 \alpha_4}{\alpha_3} \right) z_1 - \frac{\alpha_2}{\alpha_3} z_2 \\ & + \frac{2}{\alpha_3} \left\{ [2\ell(\ell+1) - 1] \alpha_1 \alpha_2 + 2[\ell(\ell+1) - 1] \alpha_1^2 \right\} z_3 \\ & + (V - 3) z_4 + 2 \frac{\alpha_1}{\alpha_3} \Delta S, \end{aligned} \quad (43)$$

where

$$U \equiv \frac{d \ln g}{d \ln r} + 2, \quad V \equiv \frac{\rho g r}{P} = -\frac{d \ln P}{d \ln r}, \quad (44)$$

$$\alpha_1 \equiv \frac{\mu}{P}, \quad \alpha_2 \equiv \Gamma - \frac{3\mu}{2P}, \quad \alpha_3 \equiv \Gamma + \frac{4\mu}{3P},$$

where g is the positive Newtonian gravitational acceleration. For the case of δT source term, we have $\Gamma = (\partial \ln P / \partial \ln \rho)|_T$, $\alpha_4 = (\partial \ln P / \partial \ln T)|_\rho (d \ln T / d \ln r)$, and $\Delta S = (\partial \ln P / \partial \ln T)|_\rho (\delta T / T)$.

We use the same boundary conditions as in Ushomirsky et al. (2000). At the interface between the core and crust, or nuclear pasta, we have

$$z_2 = Vz_1, \quad z_4 = 0. \quad (45)$$

However, at the interface between the crust and the ocean, the density may have discontinuity, and we obtain the following boundary conditions,

$$z_2 = V \frac{\rho_1}{\rho_s} z_1, \quad z_4 = 0, \quad (46)$$

where $(\rho_s - \rho_1)/\rho \approx 5 \times 10^{-5}$, ρ_s and ρ_1 are densities of elastic and liquid at the interface. Furthermore, Gittins et al. (2020) constructed a new scheme for NS mountains and modified the boundary conditions for fluid-elastic interfaces.

When we discuss the density discontinuity at the fluid-elastic interfaces, the perturbed multipole moments can be written as (Ushomirsky et al. 2000)

$$Q_{lm} = - \int_{r_{\text{bot}}}^{r_{\text{top}}} \frac{1}{V} \left\{ \ell(\ell+1)z_4 - 2\alpha_1 \left(2 \frac{dz_1}{d \ln r} + \ell(\ell+1)z_3 \right) + (\ell+4-U)(z_2 - Vz_1) \right\} r^{\ell+2} \rho dr, \quad (47)$$

where r_{top} and r_{bot} are the top and bottom of the crust. For the case of nuclear pasta, r_{bot} is the base of the nuclear pasta region. In the present work, we calculate the quadrupole moment, Q_{22} , using the above equation rigorously.

According to the results of Ushomirsky et al. (2000), the fiducial quadrupole moment Q_{fid} generated by an individual capture layer in the outer crust can be approximated as

$$Q_{\text{fid}}^{\text{outer}} \approx 1.3 \times 10^{36} \text{ g cm}^2 \times R_6^4 \left(\frac{T}{10^8 \text{ K}} \right) \left(\frac{\delta T / T}{1\%} \right) \left(\frac{E_{\text{cap}}}{30 \text{ MeV}} \right)^3, \quad (48)$$

where $R_6 = R/10^6 \text{ cm}$, and E_{cap} is the threshold energy, equivalent to the electron chemical potential μ_e at the transition between one nuclear species and the next.

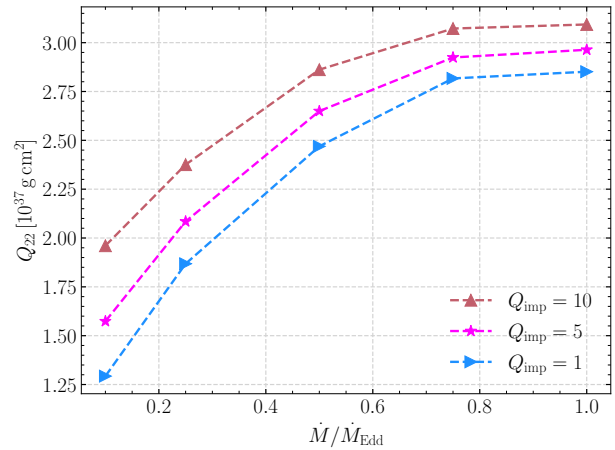


Figure 9. The absolute value of quadrupole moment as a function of the accretion rates without nuclear pasta for different impurity parameters. We set $f_{\text{nuc}} = 0.1$ and $f_{\text{comp}} = 0$.

In the inner crust, the fiducial quadrupole moment is defined as

$$Q_{\text{fid}}^{\text{inner}} \equiv \int \frac{\partial \ln \rho}{\partial \ln T} \Big|_P \frac{\delta T}{T} \rho r^{\ell+2} dr. \quad (49)$$

In particular, we can calculate the fiducial value of the quadrupole moment for nuclear pasta using Eq. (49). The fiducial value is $6.89 \times 10^{39} \text{ g cm}^2$. This value is equivalent to $1.32 \times 10^{-6} \text{ MR}^2$, where $M = 1.84 M_\odot$ and $R = 11.89 \text{ km}$.

5.2. Results: elastic deformation

In Fig. 9, we show the absolute value of quadrupole moment as a function of the accretion rates without nuclear pasta for different impurity parameters. The quadrupole moment increases with the increase of the accretion rates. The increase in impurity parameters leads to a higher quadrupole moment. We interpret this as follows. The quadrupole moment is directly proportional to the temperature perturbation, which is associated with an increase in impurity parameter (see Eq. (49) and right panel of Fig. 8). According to our results, one finds that the quadrupole moment without nuclear pasta is

$$Q_{22}^{\text{crust}} \approx 2.2 \times 10^{37} \text{ g cm}^2. \quad (50)$$

The results are in order-of-magnitude agreement with the analytical results of Jones & Hutchins (2024).

For the nuclear pasta model, we show in Fig. 10 the relation of the quadrupole moment against accretion rates. One notices that this value of the quadrupole moment is up to two orders of magnitude larger than the above case. The quadrupole moment with nuclear pasta can

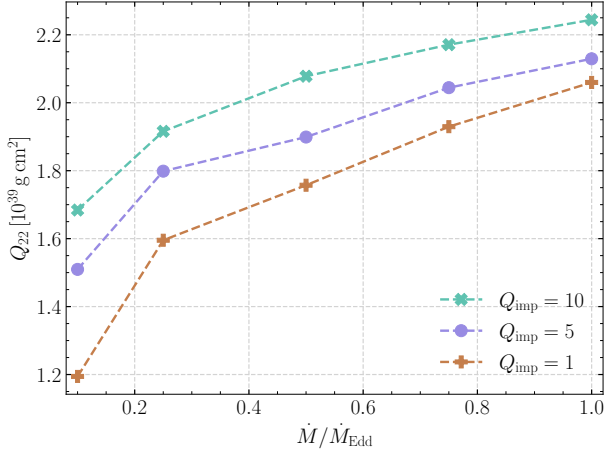


Figure 10. Same as Fig. 9, but for the effect of nuclear pasta.

be approximated by

$$Q_{22}^{\text{pasta}} \approx 1.7 \times 10^{39} \text{ g cm}^2. \quad (51)$$

Next, we discuss the detectability of known accreting NSs using the data available on the properties of the accreting NSs in LMXBs. We mainly consider two relevant categories of accreting NSs: AMXPs and the nuclear-powered X-ray pulsars (NXPs; Watts et al. 2008; Haskell et al. 2015). The details of the LMXBs we use are listed in Table 1.

In addition, a fully coherent search over time is sensitive to a strain (Jaranowski et al. 1998)

$$h_0 \approx 11.4 \sqrt{S_n(\nu)/T_{\text{obs}}}, \quad (52)$$

where $S_n(\nu)$ is the detector noise power spectral density, and the factor 11.4 accounts for a signal-to-noise ratio threshold, resulting in a single trial false alarm rate of 1% and a false dismissal rate of 10% (Abbott et al. 2007b; Watts et al. 2008; Haskell et al. 2015; Zhang et al. 2024). Detector network sensitivities are shown for advanced LIGO (adv LIGO), advanced Virgo (adv Virgo; Abbott et al. 2016), Cosmic Explorer (CE; Abbott et al. 2017b), and Einstein Telescope (ET; Punturo et al. 2010; Maggiore et al. 2020)¹.

In Fig. 11, we compare predicted results to the detectable amplitude limits. The detectable limits were obtained from Eq. (52) with $T_{\text{obs}} = 2$ year, and our results are obtained from Eq. (26), where Q_{22} is obtained from Eqs. (50) and (51), respectively. It is clear from the figure that all systems fall well below the sensitivity curves for adv LIGO and adv Virgo, with only a few sources promising detections by CE and ET.

¹ Strain sensitivity data were taken from the publicly available LIGO document at <https://dcc.ligo.org/LIGO-T1500293/public>.

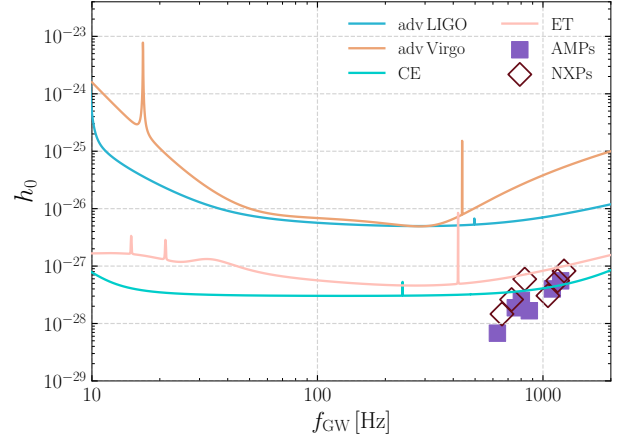


Figure 11. GW strain versus frequency for mountains in known pulsars. Closed squares denote AMXPs, and open diamonds indicate NXPs. The solid curves show the nominal strain noise sensitivity for various GW detectors. The predicted results are from Eqs. (26) and (50).

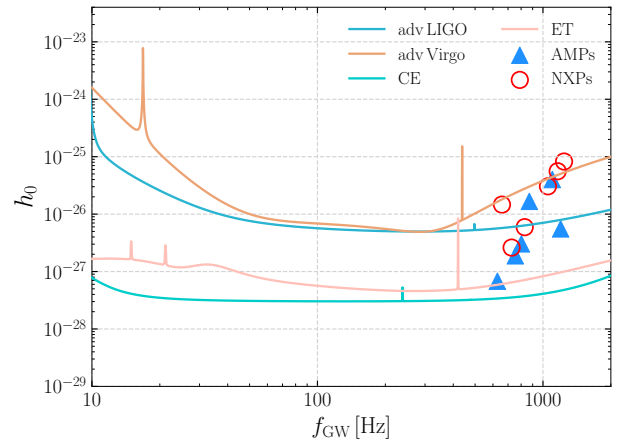


Figure 12. Similar to Fig. 11, but with the nuclear pasta effect. Closed triangles indicate AMXPs, and open circles indicate NXPs. The predicted results are from Eqs. (26) and (51).

We next discuss the effect of nuclear pasta. Our results and the detectable amplitudes are shown in Fig. 12. We can see that these sources are well above the sensitivity curves for CE and ET detectors, indicating that these sources are promising targets after considering the nuclear pasta phase.

6. BREAKING STRAIN OF THE NEUTRON STAR CRUST

The breaking properties of an NS crust have implications for the CGWs (Horowitz & Kadau 2009), magnetar outbursts (Thompson & Duncan 2001), resonant crust shattering in NS mergers (Tsang et al. 2012), and pulsar glitches (Ruderman 1969). Molecular dynamic sim-

Table 1. Estimated spin frequency ν , distance, outburst duration, and the long-term flux of different LMXBs. Sources in the top half of the table are AMXPs, while those in the bottom half are NXPs.

Source	ν (Hz)	Distance (kpc)	Outburst duration (days)	Long-term flux F_{av} ($\times 10^{-8} \text{ erg cm}^{-2} \text{ s}^{-1}$)	Reference
AMXPs					
SAX J1808.4–3658	401	3.5	30	8.6×10^{-3}	Patruno et al. (2009)
XTE J1751–305	435	7.5	10	2.0×10^{-3}	Miller et al. (2003)
XTE J1814–338	314	8	60	1.3×10^{-3}	Haskell et al. (2015)
HETE J1900.1–2455	377	5	3000	1.8×10^{-2}	Papitto et al. (2013)
Aql X–1	550	5	30	1.2×10^{-1}	Güngör et al. (2014)
IGR J00291+5934	599	5	14	1.8×10^{-3}	Falanga et al. (2005)
NXPs					
4U 1608–52	620	3.6	700	2.5×10^{-1}	Gierlinski & Done (2002)
4U 1636–536	581	5	–	4.7×10^{-1}	Haskell et al. (2015)
4U 1702–429	329	5.5	–	1.3×10^{-1}	Haskell et al. (2015)
4U 0614+091	415	3.2	–	1.2×10^{-1}	Piraino et al. (1999)
4U 1728–34	363	5	–	2.3×10^{-1}	Egron et al. (2011)
KS 1731–260	526	7	4563	2.2×10^{-1}	Narita et al. (2001)

ulations indicate the maximum breaking stress around 0.1 (Horowitz & Kadau 2009; Hoffman & Heyl 2012). Other estimates of the breaking strain approach to 0.04 (Baiko & Chugunov 2018). Following the approach in Ushomirsky et al. (2000), we use the von Mises criterion to define the elastic yield limit. The von Mises strain is characterized by

$$\bar{\sigma}^2 \equiv \frac{1}{2} \sigma_{ij} \sigma^{ij}. \quad (53)$$

Here $\sigma_{ij} = t_{ij}/\mu$ is the strain tensor. We assume that the crust will yield when $\bar{\sigma} \geq \sigma_{\text{max}}$, where σ_{max} is the breaking strain of the crust. Using Eq. (30), the right term of the above equation can be written as (Ushomirsky et al. 2000)

$$\begin{aligned} \sigma_{ij} \sigma^{ij} = & \frac{3}{2} \sigma_{rr}^2 \text{Re}(Y_{\ell m})^2 + \sigma_{r\perp}^2 \text{Re}(f_{ij})^2 \\ & + \sigma_{\Lambda}^2 \text{Re}\left(\Lambda_{ij} + \frac{1}{2} e_{ij} Y_{\ell m}\right)^2. \end{aligned} \quad (54)$$

Here, recall that we define all variables to be real. We will calculate the individual components of the shear strain using the expressions from Eqs. (36) to (39). The individual components of the breaking strain can be written as (see Ushomirsky et al. 2000, for a detailed

variational derivation),

$$\sigma_{rr}(r) = \frac{4}{3} \frac{dz_1}{d \ln r} + \frac{2}{3} \beta^2 z_3, \quad (55)$$

$$\sigma_{r\perp}(r) = \frac{\beta^2}{\mu} z_4, \quad (56)$$

$$\sigma_{\Lambda}(r) = 2\beta^2 z_3. \quad (57)$$

Note that the rr -component of the shear strain at any point in the crust is $\sigma_{rr}(r, \theta, \phi) = \sigma_{rr}(r) \text{Re}\{Y_{\ell m}(\theta, \phi)\}$, similarly for the other components. For illustration, for $\ell = m = 2$, the maximum value of angular factor is $(15/32\pi)^{1/2} = 0.39$ for σ_{rr} , $(5/8\pi)^{1/2} = 0.45$ for $\sigma_{r\perp}$, and $(5/48\pi)^{1/2} = 0.18$ for σ_{Λ} (Ushomirsky et al. 2000).

In Fig. 13, we show the different components of the shear strain without nuclear pasta. A background model has $\dot{M} = 0.5 \dot{M}_{\text{Edd}}$, $f_{\text{nuc}} = 0.1$, and $f_{\text{comp}} = 0$, and the results of temperature perturbation are $\delta T/T = 0.85\%$ with the maximum value of the threshold energy $E_{\text{cap}} = 43.69 \text{ MeV}$. Note that the maximum value of the threshold energy is dependent on the different EOS models (Haensel & Zdunik 1990a; Fantina et al. 2018). We can see that the rr -component is larger than the other two components. Moreover, the maximum values of $\sigma_{r\perp}(r)$ and $\sigma_{\Lambda}(r)$ remain below 0.1. The results are similar to the results of Ushomirsky et al. (2000); see Figs. 19 and 20 of their work. When $\sigma_{rr}(r)$ is the dominant stress component, the expression of quadrupole moment becomes $Q_{22}^{\text{crust}} = 2.2 \times 10^{37} (\sigma_{rr}/0.01) \text{ g cm}^2$.

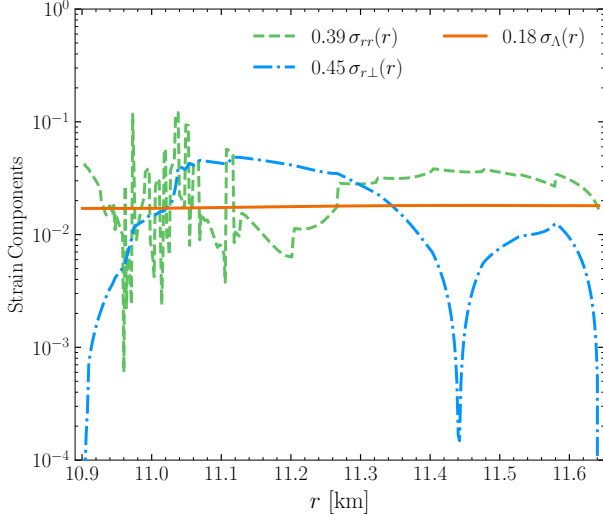


Figure 13. The maximum values of the different components of the shear strain without nuclear pasta as a function of the radius. The dashed line is $0.39 \sigma_{rr}(r)$, the dashdot line denotes $0.45 \sigma_{r\perp}(r)$, and the solid line shows $0.18 \sigma_{\Lambda}(r)$. The background model has $\dot{M} = 0.5 \dot{M}_{\text{Edd}}$, $f_{\text{nuc}} = 0.1$, and $f_{\text{comp}} = 0$.

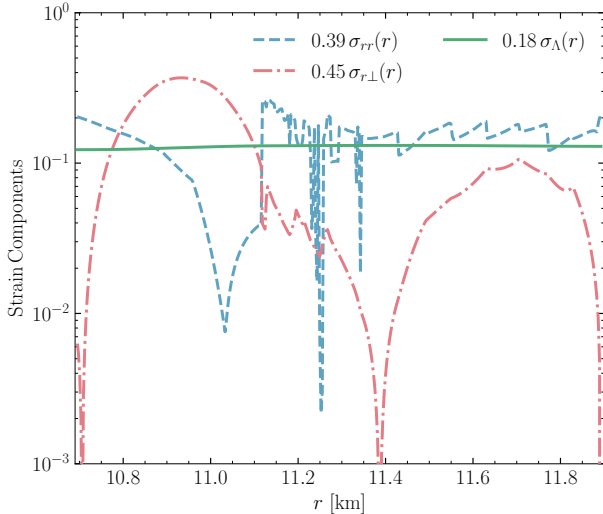


Figure 14. Same as Fig. 13, but with the effect of the nuclear pasta.

Figure 14 presents the results illustrating the nuclear pasta effect. We find that the maximum values of $\sigma_{rr}(r)$, $\sigma_{r\perp}(r)$, and $\sigma_{\Lambda}(r)$ range from 0.1 to 0.4, larger than those in the previous case without nuclear pasta. Similarly, the expression for the quadrupole moment becomes $Q_{22}^{\text{pasta}} = 1.7 \times 10^{39} (\sigma_{ij}/0.1) \text{ g cm}^2$, where σ_{ij} can take any of the three components. In particular, our results with nuclear pasta agree with previous calculations of molecular dynamic simulations (Horowitz & Kadau 2009; Hoffman & Heyl 2012; Caplan et al. 2018).

The large breaking strain should support mountains on rapidly rotating NSs which are enough to efficiently radiate CGW.

Note that the decrease in crust depth results in negative $\sigma_{r\perp}(r)$. To compare with the values of σ_{rr} and $\sigma_{\Lambda}(r)$, we plot the absolute value of $\sigma_{r\perp}(r)$ in Figs. 13 and 14.

7. SUMMARY AND DISCUSSION

In this paper, we investigated the effect of nuclear pasta on the quadrupole moments in LMXBs. We assume that the GW spin-down torque is balanced by accretion-induced spin-up torque. The quadrupole moment needed to reach this spin equilibrium is $Q_{22} = 1.7 \times 10^{39} \text{ g cm}^2$. Compared with the results of Ushomirsky et al. (2000), the quadrupole moment is up to two orders of magnitude [cf. Eq. (50)]. The main results of our work are as follows.

- (i) By expanding the computational domain in our calculations, we have introduced a more realistic representation of the thermal background of the star. We have outlined the key mechanisms of neutrino emission and thermal transport in the regions of the crust and nuclear pasta. Moreover, we discussed the effects of impurity parameters on the temperature profiles and heat flux.
- (ii) Using the thermal perturbation equations, we have found that the temperature variations can easily induce a required quadrupole moment with about 10% ($f_{\text{nuc}} = 0.1$) lateral variations of nuclear heating. We also calculated the temperature variations versus different accretion rates and impurity parameters in the nuclear pasta regions. In particular, the maximal values of $\delta T/T$ increase by a factor of two.
- (iii) Based on the crustal perturbation equations, we calculated the relationship between the quadrupole moment and the accretion rates for both regions of the crust and nuclear pasta. The quadrupole moments increase as the accretion rates increase, which is the same as the case of the nuclear pasta (see Figs. 9 and 10). In particular, the quadrupole moment is up to two orders of magnitude larger than the case without nuclear pasta.
- (iv) We studied the detectability of known accreting NSs, including AMXPs and NXPs, and compared predicted results to the detectable amplitude limits. In the case without nuclear pasta, we found

all sources that we considered fall significantly below the sensitivity curves for adv LIGO and adv Virgo detectors, with only a few sources promising detections by CE and ET (see Fig. 11). However, these sources are well above the sensitivity curves for CE and ET detectors after considering the nuclear pasta phase. Because of the nuclear pasta properties, these sources may be promising sources for next-generation GW detectors (see Fig. 12).

- (v) We calculated the maximum shear strain for a NS crust. The maximum value for the quadrupole moment scales with the maximum strain as $Q_{\max}^{\text{crust}} = 2.2 \times 10^{37} (\sigma_{\max}/0.01) \text{ g cm}^2$ (see Fig. 13). We found that, in the case of nuclear pasta, the maximum values of the shear strain range from 0.1 to 0.4, which are larger than those in the previous case. The general relation between the maximum quadrupole moment and breaking strain is expressed as $Q_{\max}^{\text{pasta}} = 1.7 \times 10^{39} (\sigma_{\max}/0.1) \text{ g cm}^2$ (see Fig. 14).

We next outline several areas where our model could be improved in future work. First, we used the EOS of Haensel & Zdunik (1990a,b) to calculate the thermal model. This could be extended to higher-density regions, which are associated with the bottom boundary. Second, we should adopt the modern EOS for accreted crust, e.g. the one provided by Fantina et al. (2018). Note that the total heat released per nucleon is probably not significantly different from the 1.33 MeV used in this work. For illustration, using a value of 1.5 MeV per nucleon (Fantina et al. 2018, 2022), Hutchins & Jones (2023) investigated the effects of magnetic fields on the thermal mountains. Third, in calculating the temperature profiles of the nuclear pasta, we have used the thermal conductivity independent of the density (see

Eq. 20). However, as the density increases, it leads to a larger thermal conductivity (Horowitz & Berry 2008), therefore, we should consider the effect of the different thermal conductivities on the temperature profiles and heat flux in future work. Finally, in our analysis, we employed the Cowling approximation, meaning we neglected the perturbation of the gravitational potential. According to the discussion by Ushomirsky et al. (2000), the quadrupole moment will enhance the result by 25–200% in the full self-consistent calculation. One shall employ a more rigorous treatment to compute the quadrupole moment in future work.

In the present work, we have studied the effect of the nuclear pasta in high-density regions on the background model, temperature perturbation, quadrupole moment, and shear strain. However, Jones & Hutchins (2024) pointed out that deep capture layers may not exist based on the EOS model of the accreted crust of Gusakov & Chugunov (2020). Hence, they discussed an alternative source of temperature, coming from the crustal lattice pressure. Furthermore, an anisotropic NS crust will produce non-axisymmetric deformations (Morales & Horowitz 2024) and support an ellipticity ranges from 10^{-9} to 10^{-8} (Morales & Horowitz 2024). These can be considered in future work.

8. ACKNOWLEDGEMENTS

We thank Zexin Hu for helpful discussions. This work was supported by the National SKA Program of China (2020SKA0120300, 2020SKA0120100), the National Natural Science Foundation of China (11991053, 12275234, 12342027), the Beijing Natural Science Foundation (1242018), the Max Planck Partner Group Program funded by the Max Planck Society, and the High-Performance Computing Platform of Peking University.

REFERENCES

- Abadie, J., et al. 2011, *ApJ*, 737, 93, doi: [10.1088/0004-637X/737/2/93](https://doi.org/10.1088/0004-637X/737/2/93)
- Abbott, B., et al. 2005, *Phys. Rev. Lett.*, 94, 181103, doi: [10.1103/PhysRevLett.94.181103](https://doi.org/10.1103/PhysRevLett.94.181103)
- . 2007a, *Phys. Rev. D*, 76, 042001, doi: [10.1103/PhysRevD.76.042001](https://doi.org/10.1103/PhysRevD.76.042001)
- . 2007b, *Phys. Rev. D*, 76, 082001, doi: [10.1103/PhysRevD.76.082001](https://doi.org/10.1103/PhysRevD.76.082001)
- Abbott, B. P., et al. 2016, *Living Rev. Rel.*, 19, 1, doi: [10.1007/s41114-020-00026-9](https://doi.org/10.1007/s41114-020-00026-9)
- . 2017a, *Phys. Rev. D*, 96, 062002, doi: [10.1103/PhysRevD.96.062002](https://doi.org/10.1103/PhysRevD.96.062002)
- . 2017b, *Class. Quant. Grav.*, 34, 044001, doi: [10.1088/1361-6382/aa51f4](https://doi.org/10.1088/1361-6382/aa51f4)
- . 2019, *Phys. Rev. D*, 100, 024004, doi: [10.1103/PhysRevD.100.024004](https://doi.org/10.1103/PhysRevD.100.024004)
- Abbott, R., et al. 2021, *Phys. Rev. D*, 104, 082004, doi: [10.1103/PhysRevD.104.082004](https://doi.org/10.1103/PhysRevD.104.082004)
- . 2022a, *Phys. Rev. D*, 105, 022002, doi: [10.1103/PhysRevD.105.022002](https://doi.org/10.1103/PhysRevD.105.022002)
- . 2022b, *Phys. Rev. D*, 106, 102008, doi: [10.1103/PhysRevD.106.102008](https://doi.org/10.1103/PhysRevD.106.102008)

- Andersson, N., Glampedakis, K., Haskell, B., & Watts, A. L. 2005, *MNRAS*, 361, 1153, doi: [10.1111/j.1365-2966.2005.09167.x](https://doi.org/10.1111/j.1365-2966.2005.09167.x)
- Andersson, N., Kokkotas, K. D., & Stergioulas, N. 1999, *ApJ*, 516, 307, doi: [10.1086/307082](https://doi.org/10.1086/307082)
- Baiko, D. A., & Chugunov, A. I. 2018, *MNRAS*, 480, 5511, doi: [10.1093/mnras/sty2259](https://doi.org/10.1093/mnras/sty2259)
- Baiko, D. A., Haensel, P., & Yakovlev, D. G. 2001, *A&A*, 374, 151, doi: [10.1051/0004-6361:20010621](https://doi.org/10.1051/0004-6361:20010621)
- Bildsten, L. 1998, *ApJL*, 501, L89, doi: [10.1086/311440](https://doi.org/10.1086/311440)
- Brown, E. F. 2000, *ApJ*, 531, 988, doi: [10.1086/308487](https://doi.org/10.1086/308487)
- Brown, E. F., & Cumming, A. 2009, *ApJ*, 698, 1020, doi: [10.1088/0004-637X/698/2/1020](https://doi.org/10.1088/0004-637X/698/2/1020)
- Caplan, M. E., Forsman, C. R., & Schneider, A. S. 2021, *Phys. Rev. C*, 103, 055810, doi: [10.1103/PhysRevC.103.055810](https://doi.org/10.1103/PhysRevC.103.055810)
- Caplan, M. E., & Horowitz, C. J. 2017, *Rev. Mod. Phys.*, 89, 041002, doi: [10.1103/RevModPhys.89.041002](https://doi.org/10.1103/RevModPhys.89.041002)
- Caplan, M. E., Schneider, A. S., & Horowitz, C. J. 2018, *Phys. Rev. Lett.*, 121, 132701, doi: [10.1103/PhysRevLett.121.132701](https://doi.org/10.1103/PhysRevLett.121.132701)
- Chakrabarty, D., Morgan, E. H., Muno, M. P., et al. 2003, *Nature*, 424, 42, doi: [10.1038/nature01732](https://doi.org/10.1038/nature01732)
- Cook, G. B., Shapiro, S. L., & Teukolsky, S. A. 1994, *ApJL*, 423, L117, doi: [10.1086/187250](https://doi.org/10.1086/187250)
- Deibel, A., Cumming, A., Brown, E. F., & Reddy, S. 2017, *ApJ*, 839, 95, doi: [10.3847/1538-4357/aa6a19](https://doi.org/10.3847/1538-4357/aa6a19)
- Dorso, C. O., Strachan, A., & Frank, G. A. 2020, *Nucl. Phys. A*, 1002, 122004, doi: [10.1016/j.nuclphysa.2020.122004](https://doi.org/10.1016/j.nuclphysa.2020.122004)
- Douchin, F., & Haensel, P. 2001, *A&A*, 380, 151, doi: [10.1051/0004-6361:20011402](https://doi.org/10.1051/0004-6361:20011402)
- Egron, E., et al. 2011, *A&A*, 530, A99, doi: [10.1051/0004-6361/201016093](https://doi.org/10.1051/0004-6361/201016093)
- Falanga, M., Kuiper, L., Poutanen, J., et al. 2005, *A&A*, 444, 15, doi: [10.1051/0004-6361:20053472](https://doi.org/10.1051/0004-6361:20053472)
- Fantina, A. F., Zdunik, J. L., Chamel, N., et al. 2018, *A&A*, 620, A105, doi: [10.1051/0004-6361/201833605](https://doi.org/10.1051/0004-6361/201833605)
- . 2022, *A&A*, 665, A74, doi: [10.1051/0004-6361/202243715](https://doi.org/10.1051/0004-6361/202243715)
- Fujisawa, K., Kisaka, S., & Kojima, Y. 2022, *MNRAS*, 516, 5196, doi: [10.1093/mnras/stac2585](https://doi.org/10.1093/mnras/stac2585)
- Galloway, D. K., Markwardt, C. B., Morgan, E. H., Chakrabarty, D., & Strohmayer, T. E. 2005, *ApJL*, 622, L45, doi: [10.1086/429563](https://doi.org/10.1086/429563)
- Gao, Y., Shao, L., Desvignes, G., et al. 2023, *MNRAS*, 519, 1080, doi: [10.1093/mnras/stac3546](https://doi.org/10.1093/mnras/stac3546)
- Gao, Y., Shao, L., Xu, R., et al. 2020, *MNRAS*, 498, 1826, doi: [10.1093/mnras/staa2476](https://doi.org/10.1093/mnras/staa2476)
- Ghosh, P., & Lamb, F. K. 1978, *ApJL*, 223, L83, doi: [10.1086/182734](https://doi.org/10.1086/182734)
- Gierlinski, M., & Done, C. 2002, *MNRAS*, 337, 1373, doi: [10.1046/j.1365-8711.2002.06009.x](https://doi.org/10.1046/j.1365-8711.2002.06009.x)
- Gittins, F., Andersson, N., & Jones, D. I. 2020, *MNRAS*, 500, 5570, doi: [10.1093/mnras/staa3635](https://doi.org/10.1093/mnras/staa3635)
- Güngör, C., Güver, T., & Ekşi, K. Y. 2014, *MNRAS*, 439, 2717, doi: [10.1093/mnras/stu128](https://doi.org/10.1093/mnras/stu128)
- Gusakov, M. E., & Chugunov, A. I. 2020, *Phys. Rev. Lett.*, 124, 191101, doi: [10.1103/PhysRevLett.124.191101](https://doi.org/10.1103/PhysRevLett.124.191101)
- Haensel, P., Kaminker, A. D., & Yakovlev, D. G. 1996, *A&A*, 314, 328. <https://arxiv.org/abs/astro-ph/9604073>
- Haensel, P., Potekhin, A. Y., & Yakovlev, D. G. 2007, *Neutron stars 1: Equation of state and structure*, Vol. 326 (New York, USA: Springer), doi: [10.1007/978-0-387-47301-7](https://doi.org/10.1007/978-0-387-47301-7)
- Haensel, P., & Zdunik, J. L. 1990a, *A&A*, 229, 117
- . 1990b, *A&A*, 227, 431
- Haskell, B., Jones, D. I., & Andersson, N. 2006, *MNRAS*, 373, 1423, doi: [10.1111/j.1365-2966.2006.10998.x](https://doi.org/10.1111/j.1365-2966.2006.10998.x)
- Haskell, B., Priymak, M., Patruno, A., et al. 2015, *MNRAS*, 450, 2393, doi: [10.1093/mnras/stv726](https://doi.org/10.1093/mnras/stv726)
- Haskell, B., Samuelsson, L., Glampedakis, K., & Andersson, N. 2008, *MNRAS*, 385, 531, doi: [10.1111/j.1365-2966.2008.12861.x](https://doi.org/10.1111/j.1365-2966.2008.12861.x)
- Heyl, J. S. 2002, *ApJL*, 574, L57, doi: [10.1086/342263](https://doi.org/10.1086/342263)
- Hoffman, K., & Heyl, J. 2012, *MNRAS*, 426, 2404, doi: [10.1111/j.1365-2966.2012.21921.x](https://doi.org/10.1111/j.1365-2966.2012.21921.x)
- Horowitz, C. J., & Berry, D. K. 2008, *Phys. Rev. C*, 78, 035806, doi: [10.1103/PhysRevC.78.035806](https://doi.org/10.1103/PhysRevC.78.035806)
- Horowitz, C. J., Berry, D. K., Briggs, C. M., et al. 2015, *Phys. Rev. Lett.*, 114, 031102, doi: [10.1103/PhysRevLett.114.031102](https://doi.org/10.1103/PhysRevLett.114.031102)
- Horowitz, C. J., & Kadau, K. 2009, *Phys. Rev. Lett.*, 102, 191102, doi: [10.1103/PhysRevLett.102.191102](https://doi.org/10.1103/PhysRevLett.102.191102)
- Hutchins, T. J., & Jones, D. I. 2023, *MNRAS*, 522, 226, doi: [10.1093/mnras/stad967](https://doi.org/10.1093/mnras/stad967)
- Jaranowski, P., Krolak, A., & Schutz, B. F. 1998, *Phys. Rev. D*, 58, 063001, doi: [10.1103/PhysRevD.58.063001](https://doi.org/10.1103/PhysRevD.58.063001)
- Jones, D. I., & Andersson, N. 2002, *MNRAS*, 331, 203, doi: [10.1046/j.1365-8711.2002.05180.x](https://doi.org/10.1046/j.1365-8711.2002.05180.x)
- Jones, D. I., & Hutchins, T. J. 2024, arXiv e-prints, arXiv:2407.00162, doi: [10.48550/arXiv.2407.00162](https://doi.org/10.48550/arXiv.2407.00162)
- Jones, D. I., & Riles, K. 2024, arXiv e-prints, arXiv:2403.02066, doi: [10.48550/arXiv.2403.02066](https://doi.org/10.48550/arXiv.2403.02066)
- Lattimer, J. M., & Prakash, M. 2007, *Phys. Rept.*, 442, 109, doi: [10.1016/j.physrep.2007.02.003](https://doi.org/10.1016/j.physrep.2007.02.003)
- Levin, Y. 1999, *ApJ*, 517, 328, doi: [10.1086/307196](https://doi.org/10.1086/307196)

- Lin, Z., Caplan, M. E., Horowitz, C. J., & Lunardini, C. 2020, *Phys. Rev. C*, 102, 045801, doi: [10.1103/PhysRevC.102.045801](https://doi.org/10.1103/PhysRevC.102.045801)
- Lopez, J. A., Dorso, C. O., & Frank, G. A. 2021, *Front. Phys. (Beijing)*, 16, 24301, doi: [10.1007/s11467-020-1004-2](https://doi.org/10.1007/s11467-020-1004-2)
- Maggiore, M., et al. 2020, *JCAP*, 03, 050, doi: [10.1088/1475-7516/2020/03/050](https://doi.org/10.1088/1475-7516/2020/03/050)
- Mahmoodifar, S., & Strohmayer, T. 2013, *ApJ*, 773, 140, doi: [10.1088/0004-637X/773/2/140](https://doi.org/10.1088/0004-637X/773/2/140)
- Melatos, A., & Payne, D. J. B. 2005, *ApJ*, 623, 1044, doi: [10.1086/428600](https://doi.org/10.1086/428600)
- Miller, J. M., Wijnands, R., Mendez, M., et al. 2003, *ApJL*, 583, L99, doi: [10.1086/368105](https://doi.org/10.1086/368105)
- Morales, J. A., & Horowitz, C. J. 2024, *Phys. Rev. D*, 110, 044016, doi: [10.1103/PhysRevD.110.044016](https://doi.org/10.1103/PhysRevD.110.044016)
- Morales, J. A., & Horowitz, C. J. 2024, arXiv e-prints, arXiv:2409.14482, doi: [10.48550/arXiv.2409.14482](https://doi.org/10.48550/arXiv.2409.14482)
- Nandi, R., & Schramm, S. 2018, *ApJ*, 852, 135, doi: [10.3847/1538-4357/aa9f12](https://doi.org/10.3847/1538-4357/aa9f12)
- Narita, T., Grindlay, J. E., & Barret, D. 2001, *ApJ*, 547, 420, doi: [10.1086/318326](https://doi.org/10.1086/318326)
- Ootes, L. S., Wijnands, R., & Page, D. 2019, *A&A*, 630, A95, doi: [10.1051/0004-6361/201936035](https://doi.org/10.1051/0004-6361/201936035)
- Osborne, E. L., & Jones, D. I. 2020, *MNRAS*, 494, 2839, doi: [10.1093/mnras/staa858](https://doi.org/10.1093/mnras/staa858)
- Papaloizou, J., & Pringle, J. E. 1978, *MNRAS*, 184, 501, doi: [10.1093/mnras/184.3.501](https://doi.org/10.1093/mnras/184.3.501)
- Papitto, A., et al. 2013, *Nature*, 501, 517, doi: [10.1038/nature12470](https://doi.org/10.1038/nature12470)
- Patruno, A. 2010, *ApJ*, 722, 909, doi: [10.1088/0004-637X/722/1/909](https://doi.org/10.1088/0004-637X/722/1/909)
- Patruno, A., Altamirano, D., Hessels, J. W. T., et al. 2009, *ApJ*, 690, 1856, doi: [10.1088/0004-637X/690/2/1856](https://doi.org/10.1088/0004-637X/690/2/1856)
- Patruno, A., Haskell, B., & Andersson, N. 2017, *ApJ*, 850, 106, doi: [10.3847/1538-4357/aa927a](https://doi.org/10.3847/1538-4357/aa927a)
- Pethick, C. J., Zhang, Z., & Kobayakov, D. N. 2020, *Phys. Rev. C*, 101, 055802, doi: [10.1103/PhysRevC.101.055802](https://doi.org/10.1103/PhysRevC.101.055802)
- Pi, C.-M., Yang, S.-H., & Zheng, X.-P. 2015, *RAA*, 15, 871, doi: [10.1088/1674-4527/15/6/009](https://doi.org/10.1088/1674-4527/15/6/009)
- Piraino, S., Santangelo, A., Ford, E. C., & Kaaret, P. 1999, *A&A*, 349, L77. <https://arxiv.org/abs/astro-ph/9910115>
- Pons, J. A., Viganò, D., & Rea, N. 2013, *Nature Phys.*, 9, 431, doi: [10.1038/nphys2640](https://doi.org/10.1038/nphys2640)
- Potekhin, A. Y., Pons, J. A., & Page, D. 2015, *Space Sci. Rev.*, 191, 239, doi: [10.1007/s11214-015-0180-9](https://doi.org/10.1007/s11214-015-0180-9)
- Punturo, M., et al. 2010, *Class. Quant. Grav.*, 27, 194002, doi: [10.1088/0264-9381/27/19/194002](https://doi.org/10.1088/0264-9381/27/19/194002)
- Reed, B. T., Deibel, A., & Horowitz, C. J. 2021, *ApJ*, 921, 89, doi: [10.3847/1538-4357/ac1c04](https://doi.org/10.3847/1538-4357/ac1c04)
- Riles, K. 2023, *Living Rev. Rel.*, 26, 3, doi: [10.1007/s41114-023-00044-3](https://doi.org/10.1007/s41114-023-00044-3)
- Ruderman, M. 1969, *nat*, 223, 597, doi: [10.1038/223597b0](https://doi.org/10.1038/223597b0)
- Schatz, H., Bildsten, L., Cumming, A., & Wiescher, M. 1999, *ApJ*, 524, 1014, doi: [10.1086/307837](https://doi.org/10.1086/307837)
- Schneider, A. S., Berry, D. K., Caplan, M. E., Horowitz, C. J., & Lin, Z. 2016, *Phys. Rev. C*, 93, 065806, doi: [10.1103/PhysRevC.93.065806](https://doi.org/10.1103/PhysRevC.93.065806)
- Shapiro, S. L., & Teukolsky, S. A. 1983, Black holes, white dwarfs, and neutron stars: The physics of compact objects, doi: [10.1002/9783527617661](https://doi.org/10.1002/9783527617661)
- Sotani, H. 2011, *MNRAS*, 417, L70, doi: [10.1111/j.1745-3933.2011.01122.x](https://doi.org/10.1111/j.1745-3933.2011.01122.x)
- Steltner, B., Papa, M. A., Eggenstein, H. B., et al. 2023, *ApJ*, 952, 55, doi: [10.3847/1538-4357/acdad4](https://doi.org/10.3847/1538-4357/acdad4)
- Thompson, C., & Duncan, R. C. 2001, *ApJ*, 561, 980, doi: [10.1086/323256](https://doi.org/10.1086/323256)
- Tripathee, A., & Riles, K. 2024, *Phys. Rev. D*, 109, 043049, doi: [10.1103/PhysRevD.109.043049](https://doi.org/10.1103/PhysRevD.109.043049)
- Tsang, D., Read, J. S., Hinderer, T., Piro, A. L., & Bondarescu, R. 2012, *Phys. Rev. Lett.*, 108, 011102, doi: [10.1103/PhysRevLett.108.011102](https://doi.org/10.1103/PhysRevLett.108.011102)
- Ushomirsky, G., Cutler, C., & Bildsten, L. 2000, *MNRAS*, 319, 902, doi: [10.1046/j.1365-8711.2000.03938.x](https://doi.org/10.1046/j.1365-8711.2000.03938.x)
- Van Den Broeck, C. 2005, *Class. Quant. Grav.*, 22, 1825, doi: [10.1088/0264-9381/22/9/022](https://doi.org/10.1088/0264-9381/22/9/022)
- Wagoner, R. V. 1984, *ApJ*, 278, 345, doi: [10.1086/161798](https://doi.org/10.1086/161798)
- Watts, A., Krishnan, B., Bildsten, L., & Schutz, B. F. 2008, *MNRAS*, 389, 839, doi: [10.1111/j.1365-2966.2008.13594.x](https://doi.org/10.1111/j.1365-2966.2008.13594.x)
- Wette, K. 2023, *Astropart. Phys.*, 153, 102880, doi: [10.1016/j.astropartphys.2023.102880](https://doi.org/10.1016/j.astropartphys.2023.102880)
- White, N. E., & Zhang, W. 1997, *ApJL*, 490, L87, doi: [10.1086/311018](https://doi.org/10.1086/311018)
- Xia, C.-J., Maruyama, T., Yasutake, N., Tatsumi, T., & Zhang, Y.-X. 2023, *Phys. Lett. B*, 839, 137769, doi: [10.1016/j.physletb.2023.137769](https://doi.org/10.1016/j.physletb.2023.137769)
- Yakovlev, D. G., Kaminker, A. D., Gnedin, O. Y., & Haensel, P. 2001, *Phys. Rept.*, 354, 1, doi: [10.1016/S0370-1573\(00\)00131-9](https://doi.org/10.1016/S0370-1573(00)00131-9)
- Yakovlev, D. G., & Urpin, V. A. 1980, *Soviet Ast.*, 24, 303
- Yim, G., Gao, Y., Kang, Y., Shao, L., & Xu, R. 2023, *MNRAS*, 527, 2379, doi: [10.1093/mnras/stad3337](https://doi.org/10.1093/mnras/stad3337)
- Yim, G., Shao, L., & Xu, R. 2024, *MNRAS*, 532, 3893, doi: [10.1093/mnras/stae1659](https://doi.org/10.1093/mnras/stae1659)
- Zhang, S.-R., Yuan, Y.-F., Wang, J.-M., & Ho, L. C. 2024, *MNRAS*, 532, 4550, doi: [10.1093/mnras/stae1780](https://doi.org/10.1093/mnras/stae1780)